International Journal of Applied Power Engineering (IJAPE)
Vol. 15, No. 1, March 2026, pp. 328∼351
ISSN: 2252-8792, DOI: 10.11591/ijape.v15.i1.pp328-351

Constrained multi-objective optimization of high frequency transformer design for dual active bridge converter in solid state transformers using genetic algorithms

Jayrajsinh B. Solanki[1], Kalpesh J. Chudasama[2]
[1]Electrical Engineering, Gujarat Technological University, Ahmedabad, India
[2]Electrical Engineering Department, A D Patel Institute of Technology, CVM University, Anand, India

Article Info

Article history:

Received May 16, 2025
Revised Dec 20, 2025
Accepted Jan 9, 2026

Keywords:

Dual active bridge converter
GA-based HFT design
High-frequency transformer
Multi-objective optimization
Solid-state transformer

ABSTRACT

This study presents a novel multi-constraint and multi-objective optimization based approach that applies genetic algorithms (GAs) for developing high-frequency transformer (HFT) designs for dual active bridge converters (DABs) in solid-state transformers (SSTs). SSTs are increasingly adopted in modern power systems due to their higher efficiency, compact structure, and improved operational reliability when compared with conventional transformers. Developing HFTs for SSTs involves several challenges, particularly the need to balance competing objectives such as improving efficiency, limiting losses, and reducing the area product while satisfying multiple design constraints. To address these challenges, this work applies a constrained multi-objective GA implemented in MATLAB to optimize the design of an HFT for a DAB converter. The methodology allows for the simultaneous optimization of multiple design objectives while taking into consideration restrictions like efficiency, leakage inductance, temperature limits, core winding area, and sizes. Our comparison with particle swarm optimization (PSO) indicates that the GA achieves more consistent convergence and consistently lower total losses. The case studies reinforce this observation, giving compact and high-performance HFT designs tailored for SST applications. The optimization approach provides a reliable and scalable method for developing thermally robust and space-efficient HFTs suitable for next-generation SST platforms and renewable-energy applications.

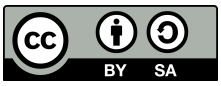

Corresponding Author:

Kalpesh J. Chudasama
Electrical Engineering Department, A D Patel Institute of Technology, CVM University
Anand, Gujarat, India
Email: ee.kalpesh.chudasama@adit.ac.in

1. INTRODUCTION

Modern power systems are shifting toward higher efficiency, reduced size, and more intelligent energy management, largely driven by the expansion of renewable sources, electric vehicle (EV) charging infrastructure, and ongoing grid upgrades. Solid-state transformers (SSTs) depart sharply from traditional magnetic-core transformer designs and introduce a fundamentally new way of handling power distribution. The inception of power electronics and semiconductor materials enabled the development of SSTs, which can switch at high frequencies while maintaining efficient energy management. SSTs are lighter and occupy significantly less space than conventional transformers. These transformers are suitable for electric vehicle

charging stations and renewable energy systems. SSTs are increasingly proposed for EV fast-charging architectures due to their modular high-frequency isolated stages and bidirectional control. Furthermore, SSTs offer advanced capabilities such as precise voltage and power flow control, thereby enhancing power system reliability and efficiency. At the core of SSTs is the high-frequency transformer (HFT), which is responsible for both power transfer and electrical isolation [1]–[6].

Recent studies highlight the role of SSTs as smart transformers (STs) which is enhancing grid flexibility and microgrid performance. ST-based microgrids optimized through genetic algorithms have shown improved voltage regulation, power quality, and fault resilience. These results indicate a broader shift from conventional transformer operation toward more intelligent transformer systems in modern power systems [7], [8]. They also underline the need for well-optimized high-frequency transformers as the main elements responsible for electrical isolation and power transfer in solid-state transformer architectures. Designing an HFT for efficient high-frequency operation is not straightforward. Thermal behavior and magnetic stability must be addressed simultaneously, which makes the problem inherently multidisciplinary within power electronics [9], [10].

Figure 1 presents the three-stage configuration of a SST. It comprises: (i) an AC-DC rectification stage, (ii) a high-frequency isolated DC-DC conversion stage using a DAB, and (iii) a final DC-AC inverter stage. Conventional distribution transformers show inherent limitations in voltage regulation, harmonic mitigation, and the handling of bidirectional power transfer. These limitations are addressed in solid-state transformers through advanced control strategies. Operating at higher frequencies helps mitigate these challenges while improving power quality and supporting stable grid interaction.

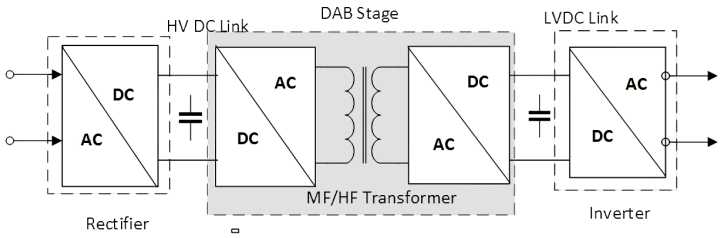

Figure 1. Three-stage SST configuration [11]

The performance of high-frequency transformers depends strongly on the materials and technologies used in their construction. Transformer efficiency and power density mainly depend on the core materials and winding design. Therefore, nanocrystalline cores are considered due to their superior magnetic characteristics that distinguish them from more typical materials such as silicon steel and ferrite cores. High-frequency operation also affects the performance, flexibility, and reliability of SSTs. It requires careful attention to insulation requirements and the leakage inductance of the HFT [12]–[14]. Additionally, accurate modeling of the phase-shifted full-bridge (PS-FB) ZVS DC-DC converter is critical in SST systems. Studies on isolated dual active bridge converter (DAB)-based converter topologies report that leakage inductance and switching stress introduce measurable efficiency and cost penalties, particularly under high-frequency operation, which motivates the inclusion of explicit leakage and thermal constraints during the optimization stage [15].

A recent study highlights the advantages of using system identification techniques over traditional averaging models, enabling more precise modelling by incorporating parasitic elements and improving dynamic performance prediction [16]. Design methodologies for HFT are being developed to improve these aspects, maintaining that the transformers are capable of handling the requirements of high-power and high-frequency functioning for a SST. It is presented that controlling the leakage inductance inside the transformers is essential to have zero voltage switching (ZVS) without the need for extra inductors, thereby optimizing the size and weight of the HFT [17]. Soft-transition designs (e.g., zero voltage transition (ZVT)) improve efficiency in non-isolated converters; in DAB-HFT stages, controlling transformer leakage to achieve ZVS provides analogous benefits without auxiliary inductors [18], [19].

There is a trade-off between the cost of material, power density and thermal efficiency. High density of power is essential because it reduces the transformer's size and weight of core and windings, which is especially useful in space-constrained situations. Higher power densities, on the other hand, generate more heat, which must be efficiently handled to avoid depreciation of transformer performance and its

life (SSTs) [20]. Several studies have explored transformer optimization using genetic algorithms (GAs) and other evolutionary techniques. Hoang and Wang [21] proposed a GA-based method for optimizing HFTs, but did not consider leakage inductance constraints. Similarly, Mogorovic and Dujic [17] focused on medium-frequency transformer optimization but did not incorporate temperature rise constraints and thermal limitations. In contrast, our approach considers multi-objective constraints like efficiency, leakage inductance, temperature rise, and winding area, which makes it more suitable for HFT applications in SSTs. Hassan and Hameed [22] studied how core geometry affects transformer efficiency using MATLAB-based graphical tools for high-frequency transformer design. Their work shows that both core shape and material choice need to be included when developing optimization frameworks. Physical and technological constraints limit the development of HFTs for SSTs for the future smart grid. Thermal capability is a major concern. As operating frequency increases, losses in the core and windings raise the operating temperature. This issue is commonly observed during design iterations. Thermal management can reduce these effects, but it increases design complexity and overall system cost. HFT design for SSTs involves balancing electromagnetic performance, thermal limits, economic considerations, and implementation constraints. Olowu *et al.* [23] proposed a multiphysics optimization framework, although their work is focused mainly on medium-frequency transformers used in distribution systems. Extending such multiphysics and multi-objective optimization approaches to HFTs allows electromagnetic, thermal, and structural constraints to be treated in a unified design process for SST applications.

Bahmani [24], [25] proposed geometric design optimization strategies but lacked multi-objective constraint handling. HFT optimization involves carefully regulating leakage inductance, winding topologies to reduce losses, and core choices based on Area product. These design improvements of transformer help to provide more efficient ZVS operation, reduce alternating current (AC) losses to maximizes efficiency, and improving thermal performance [20], [21], [24]. This work presents the design of compact, optimized, and high-efficiency transformers for modern power electronics applications, such as DAB converters and high-power conversion systems, by incorporating advanced optimization approaches in MATLAB. The design of high-frequency transformers for solid-state transformer applications involves strong coupling between electromagnetic, thermal, and material-dependent effects, which must be addressed simultaneously to ensure reliable operation [26]. Recent advances also explore AI-assisted or thermally coupled optimization for medium-frequency transformers [27], [28].

Building upon prior research in this area,the reviewed studies demonstrate steady progress in the optimization of HFTs for power electronic converters. While earlier works such as Wang *et al.* [29] and Hernández *et al.* [30] established multi-objective frameworks using NSGA-II and NSGA-III with electromagnetic modeling, they did not explicitly integrate manufacturing or thermal constraints. More recent efforts, including Shi *et al.* [31] and Su *et al.* [32], incorporated artificial intelligent (AI)-assisted or robust optimization strategies but mainly addressed distribution-level or low-frequency designs. Hashemzadeh *et al.* [33] demonstrated a DAB-based SST experimentally, yet lacked a generalized optimization procedure for transformer parameter synthesis. In contrast, the present work introduces a constrained multi-objective GA framework that simultaneously considers efficiency, copper and core losses, leakage inductance, temperature rise, and window utilization. This unified approach links electromagnetic behavior, thermal limits, and manufacturability constraints within a single design flow. Combining these domains provides a clear path toward compact, high-efficiency ,high-frequency transformers for dual-active-bridge stages in next-generation solid-state transformers.

Designing high-frequency transformers for solid-state transformer applications requires a clear understanding of the governing parameters and the constraints imposed by practical implementation. From the initial design stages, emphasis is placed on identifying the relevant parameters, governing equations, and design criteria, as summarized in section 2. This phase involves careful selection of core and winding materials, detailed estimation of total HFT losses, and the use of appropriate optimization procedures. Section 3 then addresses the key design constraints that must be satisfied to obtain feasible solutions, including efficiency requirements, limits on leakage inductance, allowable temperature rise, and winding area constraints for both primary and secondary sides, all of which directly influence manufacturability and construction feasibility. The study subsequently examines the use of genetic algorithms for constrained multi-objective optimization within a MATLAB environment. The results and discussion section reports the simulation outcomes, including Pareto-optimal fronts, which capture the inherent trade-offs among key design objectives such as area product, efficiency, and total losses.

The framework is implemented in MATLAB and verified using case studies based on a dual active bridge converter. Its performance is evaluated through comparison with particle swarm optimization during the validation stage to assess efficiency. The same optimization approach is applicable to modular solid-state transformer configurations used for renewable energy integration, where power density and isolation requirements are critical. The major contributions of this paper are summarized as follows:

- Development of a constrained multi-objective GA framework that integrates electromagnetic, thermal, and manufacturing limits within a single optimization process.
- Inclusion of leakage-inductance and temperature-rise constraints to ensure ZVS operation and thermal reliability.
- Quantitative comparison between GA and particle swarm optimization (PSO) methods under identical design objectives.
- Validation of the optimized design through MATLAB-based DAB converter simulation demonstrating high efficiency and compactness.

2. DESIGN METHODOLOGY OF HIGH FREQUENCY TRANSFORMER

The method combines standard transformer design equations with a coordinated handling of key constraints. These include efficiency, leakage inductance, thermal limits, and winding window utilization within a genetic algorithm framework. From the design iterations, the main inputs are the required power rating and the primary and secondary voltage levels. Core material properties, such as saturation flux density and permeability, along with insulation requirements, are also considered. The governing equations determine the number of primary turns, leakage inductance, core geometry, and individual loss components. During optimization runs in MATLAB, variables such as flux density, operating frequency, and current density are adjusted to meet the target performance. This approach balances electromagnetic objectives with practical constraints related to manufacturability and thermal stability.

Following the main criteria consideration while designing HFT [11]: (i) selection of material for the core and winding, (ii) winding arrangement, (iii) temperature rise considerations, (iv) magnetization and leakage inductance requirement, (v) transformer core loss calculation, and (vi) isolation requirement. Optimizing the HFT design criteria is necessary to achieve high efficiency while reducing both core losses and power converter losses. The value of optimum flux density B_{opt} is compared with the value of saturation flux density B_{sat}. So the increased value of B_{opt} such that it does not affect the efficiency of the transformer, but it can increase power density. Figure 2 depicts the optimized HFT design workflow, starting from the definition of electrical and magnetic input parameters and proceeding through constrained optimization, dimensional calculations, and efficiency validation. The sequence incorporates checks on loss minimization, thermal stability, and leakage inductance requirements to guide the selection of an HFT configuration that balances efficiency, reliability, and manufacturability.

2.1. Core material and dimension

Choosing an appropriate core material for high-frequency transformers requires a careful balance between achievable flux density and overall efficiency under practical operating constraints. Nanocrystalline cores are widely reported in the literature because of their low core losses and high saturation flux density, which make them suitable for HFT applications [24]. In practical high-power designs, however, their use is often limited by manufacturing cost and by the restricted range of available geometries, since these materials are commonly supplied in toroidal tape-wound forms. Addressing these material and geometric constraints requires careful thermal management and appropriate winding configurations to support higher power densities while maintaining compact size.

The area product (A_p) is adopted as the primary parameter for core sizing and is evaluated using established transformer design equations to satisfy both magnetic and thermal constraints. Empirical values of flux density and window utilization are applied during the core selection process, guided by manufacturer datasheets. The area product (A_p) is computed using the standard expression reported in [34].

$$A_p = \left(\frac{\sqrt{2} \sum VA}{k_v f B_0 k_t k_f \sqrt{k_u \Delta T}} \right)^{\frac{8}{7}} \tag{1}$$

Where A_p is the area product (m^4), A_c the effective core cross-sectional area (m^2), A_w the winding window area (m^2), $\sum VA$ the apparent power rating of the transformer (VA), k_u the window utilization (fill) factor, k_f the waveform factor (e.g., 4.44 for sinusoidal EMF), B_0 optimum flux density (T), and f switching frequency (Hz). The (1) calculates the product of the window area and the cross-sectional area of the core, crucial for determining the physical size of the transformer to handle the magnetic flux. Where k_t is given by (2).

$$k_t = \sqrt{\frac{h_c k_a}{\rho_w k_w}} \tag{2}$$

This criterion is used to select a core from manufacturer datasheets whose dimensions meet or exceed the calculated area product. When a single core cannot satisfy this requirement, stacked cores offer a practical means of achieving the required area product while accommodating the imposed electrical and thermal loading conditions. This approach adds flexibility to the design process and helps address limitations associated with standard core geometries and the cost of advanced magnetic materials. The core material properties listed in Table 1 illustrate the differences in loss characteristics among the available options.

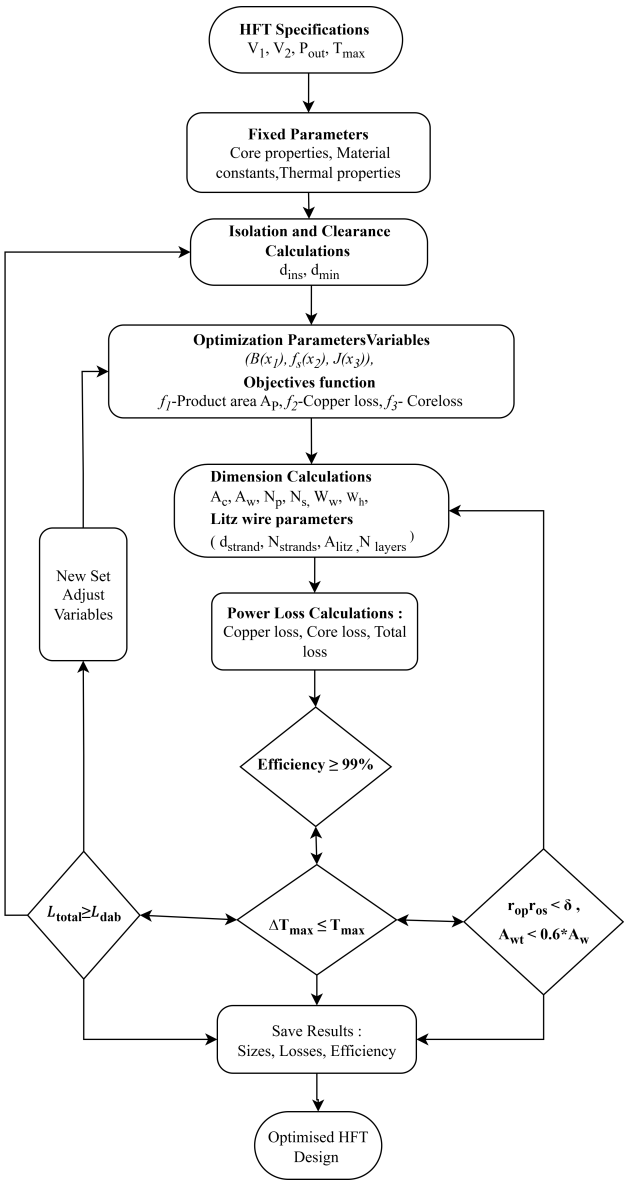

Figure 2. Flowchart of optimization-based HFT design

Both ferrite and nanocrystalline core options are examined during the design stage. Ferrite materials exhibit low core losses at frequencies above 20 kHz. However, their relatively low saturation flux density limits the achievable power density. Nanocrystalline materials provide higher permeability and higher saturation flux density. This allows a smaller magnetic volume and more effective utilization in the moderate frequency range of 10–20 kHz. Based on these trade-offs, a nanocrystalline core was selected for operation at 11 kHz, offering a practical balance between compact size, acceptable thermal behavior, and robust magnetic performance.

Table 1 lists the Steinmetz parameters k, α, and β in mW/cm^3. These parameters are normalized per unit core volume. In the loss model as (3).

$$P_{fe} = k\, V_c\, f^{\alpha} B_m^{\beta}, \tag{3}$$

k is interpreted as a volumetric loss coefficient and V_c (m^3) is the physical core volume, ensuring dimensional consistency. During optimization, the nanocrystalline parameter set ($k = 8.03$, $\alpha = 1.62$, $\beta = 1.98$) is employed in all final GA runs, while ferrite and amorphous data were used in preliminary sensitivity checks to verify material-dependent behavior. This clarification aligns the units and confirms that all core-loss calculations are performed on a per-volume basis.

Table 1. Core material properties

Material	k (mW/cm^3)	α	β
Ferrite	42.8	1.53	2.98
Silicon steel	278.4	1.39	1.80
Amorphous	46.7	1.51	1.74
Nanocrystalline	8.03	1.62	1.98

2.2. Winding material and arrangement

Winding arrangements are optimized using litz or foil conductors, depending on current levels. The design balances AC resistance with thermal handling and fill factor. The winding window utilization is constrained below 60% to ensure adequate cooling and prevent insulation failure.

To have proper design of high voltage (HV) and low voltage (LV) windings of HFT, a trade-off between several parameters should be considered: effective utilization of winding area, low losses, proper electrical isolation, and good thermal behavior. Large currents require a large conductor cross-section, but this leads to higher winding losses. Eddy currents at high frequencies produce a large amount of core losses and will guide the design toward reduced core thickness.

Subsequently, the primary number of turns N_p is calculated as (4).

$$N_p = \frac{V_p}{k_v k_f A_c B_{max} f} \tag{4}$$

Where V_p is the RMS primary voltage (V), f the frequency (Hz), $B_{\max}$ the peak flux density (T).

As a result, litz and foil conductors are the ideal choice for winding conductors in HFTs. The construction of a litz conductor consists of individual insulated wire strands twisted or braided together. The foil or litz wire conductors are used in the winding of HFTs to decrease eddy current loss. These insulated strands adjust all points in the cross-section of the litz conductor to spread the flux linkage and ensure uniform current distribution.

Due to the high currents in the line, foil conductors are employed in the low-voltage winding of medium-frequency transformer (MFT)/ high-frequency transformer (HFT). Thin foil conductors are thought to reduce losses due to the skin effect. To reduce proximity effect losses, the thickness of foil conductors should decrease as the number of layers increases. After selecting the core, the wire for HFT windings is chosen based on the optimal current density, estimated by GA optimization, as in (5).

$$J_o = K_t \sqrt{\frac{\Delta T}{2k_u} \cdot \frac{1}{\sqrt[8]{A_p}}} \tag{5}$$

The value of current density J_0 and the primary and secondary currents in HFT are used to calculate the required primary and secondary bare conductor areas. Due to the skin effect, the conductive winding

cross-section region must be considered. The diameter of the Standard Wire Gauge (SWG) wire should be less than the skin depth δ to minimize eddy current losses. The thickness of and equivalent wire or conductors whose resistance is equal to that of a solid conductor under skin effect is known as skin depth. The skin depth, also defined as effective depth at which current density falls to $1/e$ of its surface value due to the skin effect, is given by (6) [14], [34].

$$\delta = \sqrt{\frac{\rho}{\pi f \mu_0 \mu_r}} \tag{6}$$

Where ρ is the resistivity of the conductor (Ω·m), f is the operating frequency (Hz), and μ_0 is the permeability of free space ($4\pi \times 10^{-7}$ H/m). As a consequence, the type of wire SWG can be selected. Then the number of strands is calculated by required total area and selected area of strands with consideration of δ skin depth.

It is possible to estimate the required cross-sectional area of the primary or secondary windings from the rated current as (7).

$$A_{\text{winding}} = \frac{I}{J_0} \tag{7}$$

Where J_0 is the current density. The strand diameter is then selected to limit the skin effect at the chosen switching frequency, as (8).

$$d_{\text{strand}} = \frac{\delta}{2} \tag{8}$$

Where δ is the skin depth. The strand diameter is chosen between 0.5δ and δ to minimize eddy-current losses while maintaining manufacturability. The cross-sectional area of one strand is as (9).

$$A_{\text{strand}} = \pi \left(\frac{d_{\text{strand}}}{2} \right)^2 \tag{9}$$

The total number of strands required in the Litz bundle is as (10).

$$N_{\text{strand}} = \frac{A_{\text{winding}}}{A_{\text{strand}}} \tag{10}$$

The total copper area inside the Litz bundle is as (11).

$$A_{\text{cu}} = N_{\text{strand}} A_{\text{strand}} \tag{11}$$

However, due to inter-strand voids, varnish coating, and outer insulation, the actual bundle occupies a larger cross-sectional area A_{bundle}, related to the copper fill factor (packing efficiency) ν_{Litz} as (12) [14], [34].

$$A_{\text{bundle}} = \frac{A_{\text{cu}}}{\nu_{\text{Litz}}} \tag{12}$$

Typical packing factors for Litz wire range from 0.35 to 0.55, depending on strand construction and twist pitch. The equivalent outer diameter of the bundle, which determines the number of turns per layer, is as (13).

$$D_{\text{bundle}} = 2\sqrt{\frac{A_{\text{bundle}}}{\pi}} \tag{13}$$

The number of turns per layer is given by (14).

$$N_{\text{turns/layer}} = \frac{W_w}{D_{\text{bundle}}} \tag{14}$$

And the total number of layers required for each winding is as (15).

$$N_{\text{layers}} = \frac{N}{N_{\text{turns/layer}}} \tag{15}$$

Where W_w is the window width and N is the total number of primary or secondary turns.

Finally, the total effective winding area considering both primary and secondary coils is as (16).

$$A_{wt} = N_p A_{\text{bundle,p}} + N_s A_{\text{bundle,s}} \tag{16}$$

This formulation enforces the practical winding fill constraint ($A_{wt} < 0.6A_w$), allowing insulation thickness, void spaces, and Litz-wire bundle packing effects to be represented in a realistic manner. From a design standpoint, this constraint links the electrical requirements with thermal behavior and manufacturability. Generally it allows these three aspects to be addressed together within a multi-objective optimization approach.

For dry insulation of the MFT in DABs [35], the necessary minimum insulation distance between conductors is as (17).

$$D_{i,min} = \frac{V_{iso}}{K_{iso} E_{ins}} \tag{17}$$

Where V_{iso} represents the required isolation voltage level, E_{ins} denotes the dielectric strength of the insulation material, and K_{iso} corresponds to the safety margin specified by the manufacturer.

The core volume V_c and the winding volume V_w are defined as (18) [36].

$$V_c = l_m A_c \tag{18}$$

Where l_m = mean magnetic path length of the core (m).

$$l_m = 2(C_w + 2l) + 0.8 \times l_w \times (2 + \pi) \tag{19}$$

Where C_w denotes the cross-sectional width of the core, l represents the core cross-sectional thickness, and l_w is the winding width for the C-core sheets. Based on the geometric characteristics of the high-frequency transformer, an empirical expression is used to estimate the core volume as in (20).

$$V_c = \left(W_h + \frac{C_w}{2} + \frac{C_w}{2}\right) A_c + \left((W_w \times 4)\frac{A_c}{2}\right) \quad + \left((4 \times \frac{C_w}{2})\frac{A_c}{2}\right) + \left((2 \times W_h)\frac{A_c}{2}\right) \times 1.2 \tag{20}$$

Where C_w = core width in m, W_h = window height in m, W_w = window width in m, C_d = core depth in m.

Figure 3 shows the winding structure and geometric layout of the high-frequency transformer. This configuration is used to control leakage inductance through adjustments in core dimensions, winding placement, and insulation spacing. These structural choices directly affect ZVS operation, thermal behavior, and the overall efficiency of the transformer.

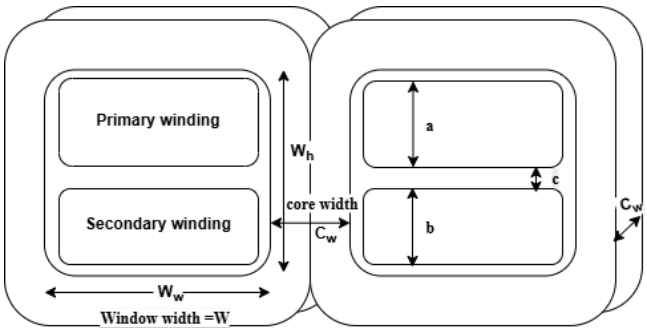

Figure 3. Cross-sectional schematic of HFT core with primary windings and secondary windings

The mean length of a turn (MLT) is calculated as (21).

$$MLT = (C_w + (W_w \times 0.4) \times 2) \times 2 + (C_d + (W_w \times 0.4) \times 2) \times 2 \tag{21}$$

A windings volume V_w is given by (22) [36].

$$V_w = MLT \times W_a \tag{22}$$

Copper loss is given by (23).

$$P_{cu} = I_p^2 R_{pac} + I_s^2 R_{sac} \tag{23}$$

Where: I_p, I_s = primary and secondary currents.

$$R_{ac} = F_R \times R_{dc} \tag{24}$$

Eddy current loss factor as (25).

$$F_R = \frac{1 + (r_0/\delta)^4}{48 + 0.8 \times (r_0/\delta)^4} \tag{25}$$

Where r_0 is the radius of the Litz wire of the primary winding and secondary windings.

The eddy current loss factor F_R [34] is used in HFT design to account for the increase in effective winding resistance due to the skin effect. Under DC conditions, the current is distributed uniformly across the conductor cross-section. At higher operating frequencies, the current concentrates near the conductor surface. This redistribution increases the effective resistance and results in additional resistive losses. F_R provides the connection between the ideal DC resistance R_{dc} and the higher AC resistance R_{ac} encountered during operation. From a winding design standpoint, this relationship is essential for limiting losses, preserving efficiency, and maintaining reliable transformer performance under high-frequency conditions.

DC resistance calculated as (26) [34].

$$R_{dc} = N \times MLT \times \ r_{20}[1 + \alpha_{20}(T_{max} - 20)] \tag{26}$$

Where:
- N is the number of turns of primary and secondary windings
- r_{20} is the tabulated resistance at 20 °C in Ω/m for the selected wire (AWG/IEC) $r_{20} = \rho_{20}/A_{\mathrm{cu}}$; the area is embedded in the wire table value [34]
- A_{cu} is the conductor cross-section (m^2)
- ρ_{20} is the resistivity of the conductor $\Omega \times \mathrm{m}$
- α_{20} is the temperature coefficient at 20 °C
- $T_{max} = T + 40$ is the maximum operating temperature.

AC resistance and proximity effects in Litz and fil windings: The previous eddy-current loss factor F_R in (25) is valid only for solid round conductors [34] and does not accurately capture proximity effects in multi-layer or litz windings. At medium-to-high frequencies, the current distribution in each layer is affected not only by the skin effect (within each strand) but also by the magnetic field of neighboring layers—the proximity effect. To account for these, the AC resistance per layer $R_{\mathrm{ac},\,i}$ is evaluated using Dowell's method [37], which models the winding as N_L stacked layers carrying uniform current in the window height. For a transformer winding of N_T total turns arranged in N_L layers, the normalized AC resistance factor is as (27).

$$\frac{R_{\mathrm{ac}}}{R_{\mathrm{dc}}} = \frac{\sinh(2y) + \sin(2y) + 2\big[\sinh^2(y) + \sin^2(y)\big](N_L^2 - 1)}{4N_L\big[\sinh(y)\cosh(y) + \sin(y)\cos(y)\big]}, \tag{27}$$

Where $y = t_{\mathrm{eff}}\sqrt{\pi f \mu_0/\rho}$, t_{eff} is the effective layer thickness of one conductor plus insulation, f is the operating frequency , μ_0 is the permeability of free space, and ρ is the resistivity of copper. The (27) is applied separately to the primary (Litz) and secondary (foil) windings to estimate their layer-dependent $R_{\mathrm{ac}}/R_{\mathrm{dc}}$ ratios. The resulting correction factors ranged from 1.06–1.12 for the Litz winding and 1.18–1.25 for the foil winding, which align with typical design curves reported in [14], [34].

For Litz wire, the AC loss is reduced because each strand's diameter d_{strand} is chosen to be smaller than the skin depth δ; however, proximity effects between bundles still occur. Hence, the bundle's effective fill factor ν_{Litz} (ratio of copper to total bundle area) is included as (28).

$$\nu_{\mathrm{Litz}} = \frac{N_{\mathrm{strand}}\pi(d_{\mathrm{strand}}/2)^2}{A_{\mathrm{bundle}}} \tag{28}$$

Where A_{bundle} accounts for varnish, twist pitch, and inter-strand voids. For commercially available Litz constructions, ν_{Litz} ranges between 0.35–0.55. The overall winding window fill factor is expressed as (29).

$$k_u = \frac{A_{\mathrm{cu,tot}}}{A_w} = \frac{\nu_{\mathrm{Litz}} N_{\mathrm{turns}} A_{\mathrm{bundle}}}{A_w} \leq 0.6, \tag{29}$$

Ensuring that insulation thickness, layer margins, and cooling clearances are respected. The copper fill fraction inside the winding itself is typically 60–70% of the bundle area after accounting for enamel and twisting; this corresponds to a total k_u of about 0.5–0.55.

Maximum flux density in the core is estimated by (30).

$$B_m = \frac{V_p \times D_T}{N_p \times A_c \times f} \tag{30}$$

Where: D_T is a duty cycle.

Core loss:

$$P_{fe} = k \times V_c \times f^{\alpha} B_m^{\beta} \tag{31}$$

Total power loss:

$$P_T = P_{cu} + P_{fe} \tag{32}$$

The increase in temperature degrades the transformer's performance output by disturbing its electric and magnetic parameters. Therefore, it is very important to conduct thermal analysis during the transformer's design stage and to estimate the increase in temperature [38]. Another important constraint is the temperature rise ΔT (°C) as a function of the surface area A_t (in cm^2) and P_T, the total power loss.

2.3. Thermal modeling and temperature rise estimation

The transformer temperature rise results from the total power loss $P_T = P_{cu} + P_{fe}$, which is dissipated primarily through natural convection and radiation. In practice, both copper and core losses contribute to localized heating in the windings and magnetic path, making thermal behavior strongly dependent on geometry and cooling conditions. Although detailed FEM-based thermal models are possible, empirical methods remain reliable for ferrite and nanocrystalline cores operating under similar cooling environments. Following McLyman [14] and Orenchak [39], the temperature rise is estimated as (33).

$$\Delta T = \left(\frac{P_T}{A_t} \right)^{0.833}, \qquad A_t = k_s \sqrt{A_p} \tag{33}$$

Where k_s (20)–(30) is a geometry factor. The exponent 0.833 is derived from extensive experimental correlations on ferrite E-cores under natural convection [39].

The model has been validated to within $\pm 10\%$ accuracy for ferrite transformers operating in the 20–200 kHz range [14]. For the 150 W, 11 kHz DAB prototype considered here, it yields an estimated temperature rise of $\Delta T \approx 25^{\circ}\mathrm{C}$, corresponding to a hotspot temperature of $T_{\mathrm{hot}} \approx 50^{\circ}\mathrm{C}$. This value remains well below the Class B insulation limit, supporting the use of this model as a reliable thermal constraint in the design process. Since transformer performance is governed by copper and core losses, the efficiency is evaluated directly from these components as (34).

$$\eta = \frac{P_{in} - (P_{cu} + P_{fe})}{P_{in}} \% \tag{34}$$

3. DUAL ACTIVE BRIDGE CONVERTER WITH HFT

Figure 4 illustrates the dual active bridge (DAB) converter with an integrated high-frequency transformer (HFT). Figure 4(a) shows the circuit architecture of the DAB converter, highlighting the full-bridge configurations on the high-voltage (HV) and low-voltage (LV) sides and the HFT that provides galvanic isolation and voltage level adaptation between the two ports [36]. Figure 4(b) presents the corresponding idealized voltage and current waveforms of the HFT, including the primary voltage, secondary voltage, and secondary current, which illustrate the phase-shift–controlled power transfer mechanism and the role of leakage inductance in shaping the current waveform during DAB operation.

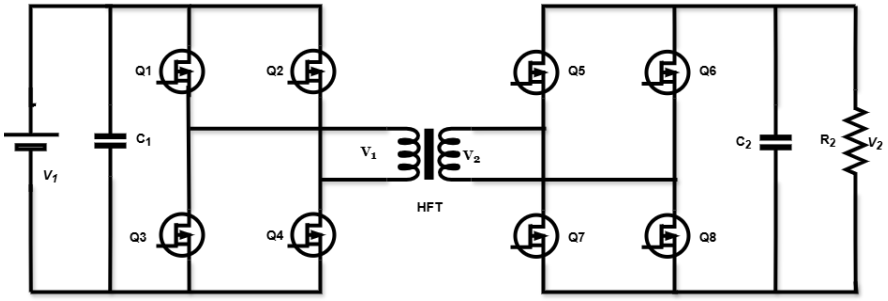

(a)

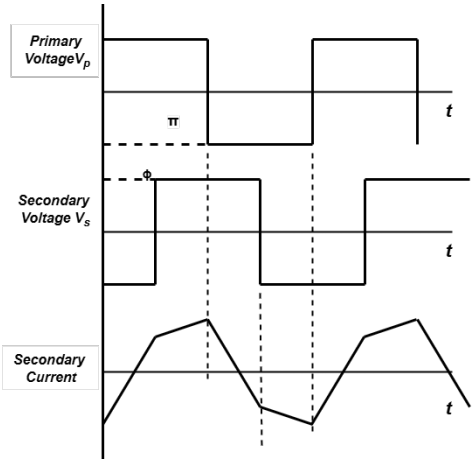

(b)

Figure 4. DAB converter with HFT waveforms [40]: (a) DAB converter and (b) HFT waveforms

In DAB converters, the leakage inductance (L_{DAB}) directly influences power transfer behavior and overall operating performance [41], [42]. The transformer within the DAB provides the required galvanic isolation and voltage matching between the high-voltage (HV) and low-voltage (LV) sides. The leakage inductance also functions as a short-term energy storage element. This stored energy shapes the current waveform and has a direct influence on switching conditions and overall converter efficiency.

For a DAB operating under single phase-shift (SPS) control, the required equivalent series inductance L_{DAB} that ensures full-power transfer and zero-voltage switching (ZVS) within the rated range can be expressed as (35) [36], [41], [43], [44].

$$L_{\mathrm{DAB}} = \frac{n\,V_1\,V_2}{2\,f_s\,P_0}\,d(1-d) \tag{35}$$

Here, L_{DAB} represents the equivalent inductance that participates in energy transfer between the two active bridges, while V_1 and V_2 denote the primary and secondary DC-link voltages, respectively. The transformer turns ratio is defined as $n = N_p/N_s$, and the converter operates at a switching frequency f_s. The rated transferred power is represented by P_0, and $d = \phi/\pi$ is the normalized phase-shift ratio ($0 < d \leq 0.5$), where

ϕ denotes the phase-shift angle between the bridge voltages. The (35) from the standard DAB power-transfer relation [36], [41], [45], [46].

$$P = \frac{n\,V_1 V_2}{\omega\,L_{\mathrm{DAB}}}\,\phi\,\left(1 - \frac{|\phi|}{\pi}\right) \tag{36}$$

By equating $P = P_0$ at the rated phase-shift $\phi = \pi d$.

Transformer leakage inductance depends greatly on the winding structure and the number of turns. The leakage inductance of the transformer is given based on the transformer's geometric parameters. Two opposite winding combinations are considered to change the level of the transformer's leakage magnetic flux. Transformer leakage inductance is critical for ZVS operation in DAB converters. Analytical formulas are used to compute leakage inductance based on core & winding geometry [14], [34], [36].

$$L_k = \mu_0 N^2 \mathrm{MLT} \frac{(a + b + 3c)}{3w} \tag{37}$$

Where μ_0 is the air permeability, N is the number of turns of windings for which the leakage inductance is being calculated for primary or secondary windings, MLT is the mean length of a turn of windings, a and b are the width of the primary and secondary windings, respectively, and c is the isolation distance between the windings, while w is the core window width.

The total height of the windings is calculated by multiplying the number of layers by the effective diameter of the litz wire for each winding. For the primary winding, the height a is given by (38).

$$a = N_{\text{layers, primary}} \cdot D_{\mathrm{bundle,Primary}} \tag{38}$$

For the secondary winding, the height b is as (39).

$$b = N_{\text{layers, secondary}} \cdot D_{\mathrm{bundle,Secondary}} \tag{39}$$

To ensure that the insulation gap meets the minimum requirement, the gap c is determined by (40).

$$c = d = W_h - (a + b) \tag{40}$$

$$d = D_{i,\text{min}} \tag{41}$$

The effective width w is then selected by ensuring it is not greater than the physical window width W_w and is at least the larger of the two horizontal widths of primary and secondary.

With primary and secondary leakage inductances L_{k_p} and L_{k_s} (each measured on its own winding), The total HFT leakage inductance referred to the secondary side is as (42).

$$L_{\text{Total}} = L_{k_p/n^2} + L_{k_s} \tag{42}$$

In each winding arrangement, the air-gap length and cross-sectional area of the leakage flux path, the transformer can be built to regulate the leakage inductance through the number of turns.

4. GENETIC ALGORITHMS (GA) AND PARTICLE SWARM OPTIMIZATION (PSO)

GAs are a fascinating and powerful type of optimization technique inspired by the process of natural selection. Genetic algorithms are chosen for their ability to explore large design spaces and avoid local minima—particularly important in the highly non-linear optimization of HFTs. Traditional gradient-based or brute-force techniques are either too slow or fail under multi-constraint environment problems.

4.1. Basics of genetic algorithms

Genetic algorithms operate by creating a population of potential solutions to a given problem, represented by a set of parameters. These algorithms simulate the process of natural evolution through operations such as selection, crossover (or recombination), and mutation.

– Selection: Choosing the fittest individuals in a population to create offspring for the next generation. Fitness is determined by how well an individual solves the problem at hand.
– Crossover: Genetic information from two parent solutions is combined to generate new offspring. This operation promotes information exchange within population and can lead to improved candidate solutions.
– Mutation: Small random changes are applied to selected genes to maintain population diversity. This step helps algorithm explore a broader search space and reduces likelihood of convergence to local minima.

These steps are repeated over successive generations until the population converges toward an optimal solution.

4.2. Multi-objective optimization with genetic algorithms

Multi-objective optimization considers multiple competing objectives subject to specified constraints. In complex engineering problems such as high-frequency transformer design, traditional gradient-based methods often fail to locate the global optimum due to the highly non-linear and discontinuous nature of the search space. Genetic algorithms are appropriate for this class of problems because they maintain a diverse population of solutions, which supports the exploration of trade-offs among objectives. In this context, GAs aim to identify a set of Pareto-optimal solutions. Within this set, improvement in one objective is possible only at the expense of at least one other objective. The resulting Pareto front represents the range of feasible trade-offs available for the optimization problem.

4.3. Constrained optimization techniques

Constrained optimization addresses problems in which the feasible solutions are restricted by explicit constraints. Genetic algorithms manage these constraints using the following techniques:

– Penalty methods: Introducing a penalty to the fitness function for constraint violations. The severity of the penalty can vary depending on the nature of the violation.
– Repair functions: Modifying infeasible solutions to make them feasible, often used in conjunction with other genetic operators like mutation and crossover.
– Using a separate population for feasible solutions: Maintaining a subset of the population that only includes feasible solutions, which can help preserve good solutions that meet the constraints.

Genetic algorithms are especially useful for problems where the search space is vast, complex, or poorly understood, making traditional search and optimization strategies ineffective. They are commonly used in engineering, economics, and other fields to develop solutions suitable for complex situations with numerous objectives and constraints.

4.4. Particle swarm optimization (PSO)

PSO is a bio-inspired population-based algorithm that simulates the social behavior of bird flocking or fish schooling. Each solution, known as a "particle," moves through the search space with a velocity dynamically adjusted based on its own and its neighbors' best-known positions. Unlike GA, which relies on evolutionary operations like crossover and mutation, PSO explores the search space using position and velocity updates, typically resulting in faster convergence. In this study, the PSO algorithm is executed in MATLAB under the same design constraints and objective functions as GA. The PSO settings included a swarm size of 50, an inertia weight of 0.7, cognitive and social coefficients set to 1.5, and a maximum of 150 generations.

5. OBJECTIVES VARIABLES AND FUNCTIONS, AND CONSTRAINTS

5.1. Optimization variables and bounds

We optimize three design variables $\mathbf{x} = [x_1\ x_2\ x_3]^\top = [B_{max}\ f_s\ J_0]^\top$, where B_{max} is peak flux density (T), f_s is switching frequency (Hz), and J_0 is current density (A/mm^2). These specific parameters are selected as primary decision variables because they directly govern the core volume, winding losses, and overall thermal performance of the transformer. Establishing these boundaries is critical to avoid magnetic saturation and to ensure that the final design remains physically manufacturable. The feasible search ranges for each variable are summarized in Table 2.

Table 2. Decision variables and bounds

Variable	Symbol	Units	Bounds
Flux density	$B_{\max}$	T	$0.10 \leq B_{\max} \leq 1.2$
Switching frequency	f_s	kHz	$10 \leq f_s \leq 60$
Current density	J_0	A/mm^2	$2.0 \leq J_0 \leq 6.0$

5.2. Objective functions

In the GA-based optimization of the HFT design, the objective is to balance the area product (f_1), copper loss (f_2), and iron loss (f_3) under practical design constraints. During the optimization runs, parameters such as flux density (x_1), operating frequency (x_2), and current density (x_3) are allowed to vary, but only within their permissible limits. This formulation reflects the trade-offs encountered in practice when targeting compact geometry, low losses, and reliable operating margins.

The area product determines the size of the transformer and is formulated as (43).

$$f_1 = \left[\frac{\sqrt{2} \sum VA}{k_v x_2 x_1 k_t k_f \sqrt{k_u \Delta T}} \right]^{\frac{8}{7}} \tag{43}$$

The objective is to minimize f_1, ensuring a compact and efficient transformer design.

Copper loss occurs due to resistance in the windings and is given by (44).

$$f_2 = I_p^2 R_{pac} + I_s^2 R_{sac} \tag{44}$$

Here R_{ac} is computed with the adopted Dowell/Litz model (proximity+skin).

Iron loss (or core loss) is the combination of hysteresis and eddy current losses, given by (45).

$$f_3 = k V_c x_2^{\alpha} B_m^{\beta} \tag{45}$$

The goal of this function is to minimize f_2 and f_3, reducing power loss, improving efficiency, and ensuring reduced heat generation and energy dissipation. The multi-objective vector is $f(x) = [f_1 \ f_2 \ f_3]^{\top}$ with:

$$f_1 = A_p(\mathbf{x}) \ \ [\mathrm{m}^4], \quad f_2 = P_{cu}(\mathbf{x}) \ \ [\mathrm{W}], \quad f_3 = P_{fe}(\mathbf{x}) \ \ [\mathrm{W}]$$

5.3. GA/PSO settings and fair-comparison protocol

The genetic algorithm (GA) is configured with a population size of $N_{pop} = 50$ and evolves over a maximum of $G = 150$ generations. The evolutionary process utilizes simulated binary crossover (SBX) with a probability of $p_c = 0.8$ and a distribution index of $\eta_c = 15$, followed by polynomial mutation with $p_m = 0.03$ and $\eta_m = 20$. This configuration results in a total computational budget of 7,500 function evaluations (FEs), calculated as $N_{pop} \times G$.

The PSO employs a swarm size of $N_{sw} = 50$ and an inertia weight of $w = 0.7$ to effectively balance global and local search capabilities. The cognitive and social acceleration coefficients are both set to $c_1 = c_2 = 1.5$, and the algorithm runs for $I = 150$ iterations with velocity clamping enabled to prevent divergence. The total number of function evaluations is maintained at $N_{sw} \times I = 7,500$ to ensure a strictly fair computational comparison with the GA.

Convergence histories: We evaluate the optimization trajectory by reporting the mean best values for the objectives f_1, f_2, and f_3 as a function of the number of function evaluations. The hypervolume metric is also monitored throughout the process to assess the quality and diversity of the Pareto front approximations over time. Additionally, we track the fraction of feasible individuals at each generation to verify the algorithm's ability to satisfy the imposed design constraints.

Multiple runs: To account for the stochastic nature of meta-heuristic algorithms, both GA and PSO are executed for $N_{runs} = 20$ independent trials using distinct random seeds. The statistical performance, calculated as the mean $\pm$ standard deviation of the objective values $\{f_1, f_2, f_3\}$ for the best feasible solution found in each run, is summarized in Table 3. Furthermore, the feasibility rate is calculated to determine the percentage of runs that successfully locate at least one valid design within the search space.

Table 3. Twenty-run statistics (best feasible per run; same FE budget)

Method	f_1 (m^4)	f_2 (W)	f_3 (W)	Feasible runs (%)
GA	$\mu \pm \sigma$	$\mu \pm \sigma$	$\mu \pm \sigma$	100
PSO	$\mu \pm \sigma$	$\mu \pm \sigma$	$\mu \pm \sigma$	95

5.4. Constraints

In the context of engineering optimization, constraints serve a fundamental role by defining the boundaries between theoretical mathematical solutions and physically realizable designs. Within the proposed genetic algorithm framework for HFT synthesis, strictly enforcing these boundaries is essential to guarantee operational reliability. Therefore, various constraints are integrated into the optimization process to ensure the final design complies with critical electrical, thermal, and geometric specifications.

The first constraint is efficiency. For instance, a constraint might specify that the efficiency of the transformer must be greater than or equal to a certain threshold value (e.g., 99%):

$$\text{Efficiency} \geq 99\% \tag{46}$$

efficiency is a key performance indicator in transformer design, as it quantifies how effectively the input power is converted into useful output power. In practical optimization studies, a minimum efficiency constraint is imposed to ensure that the resulting design operates within acceptable loss limits.

Inductance is another critical design parameter, as it directly affects voltage regulation and impedance matching. Inductance constraints are imposed to ensure that the designed transformer provides the required inductance level for DAB converter operation across the intended frequency range. This parameter is treated as a constraint during optimization to maintain compatibility with soft-switching conditions.

$$L_{Total} \geq L_{DAB} \tag{47}$$

Leakage inductance represents the portion of inductance that does not directly contribute to energy transfer between the primary and secondary windings. Constraints on leakage inductance are therefore applied to keep its value within acceptable limits, limiting excess energy storage and associated losses. During optimization, this constraint helps balance efficient power transfer with the requirements of ZVS operation and application-specific performance targets.

Constraints on temperature rise ensure that the transformer operates within safe temperature limits under specified operating conditions. Temperature rise is a critical consideration in transformer design, since excessive heating accelerates insulation ageing and degrades long-term reliability. A temperature-rise constraint is enforced to keep operating temperatures within allowable limits and to prevent thermal overstress.

$$\Delta T \leq T_{max} \tag{48}$$

In GA-based HFT design, this requirement is addressed indirectly by limiting the effective winding area to less than 60% of the available window area, which promotes adequate cooling and reduces risk of insulation failure.

$$A_{wt} < 0.6\, A_w \tag{49}$$

This constraint prevents winding overcrowding, preserves insulation clearances, and supports effective heat dissipation. It also contributes to controlled flux density levels and acceptable leakage inductance, both of which are important for stable operation. From the design iterations, enforcing this limit leads to layouts that are thermally manageable and practically manufacturable.

To limit skin-effect losses, the radii of the primary and secondary conductors are constrained to remain smaller than the skin depth δ:

$$r_{op} \leq \delta, \quad r_{os} \leq \delta \tag{50}$$

maintaining this condition improves current distribution, reduces AC resistance, and lowers heat generation in the windings. Together, these constraints guide the optimization toward HFT designs that satisfy thermal, electrical, and safety requirements while remaining suitable for practical implementation.

During initialization, each design variable is sampled uniformly within its prescribed bounds, and all derived quantities, including winding turns, window fill factor, and leakage inductance, are recomputed for each candidate solution. We use constraint-domination and, in addition, a normalized quadratic penalty added to each objective for infeasible candidates:

$$\tilde{f}_k(\mathbf{x}) \;=\; f_k(\mathbf{x}) \;+\; \sum_i \lambda_{k,i} \Big(\max\{0,\; \hat{g}_i(\mathbf{x})\} \Big)^2$$

where $\hat{g}_i$ is the constraint violation normalized by its limit.

Table 4 summarizes the constraint set and corresponding penalty weights used in the optimization framework. Each constraint represents a practical design limitation associated with efficiency, thermal rise, leakage inductance matching, window utilization, and insulation clearances. The normalized constraint violation $\hat{g}_i$ ensures that different physical quantities are treated consistently, while the penalty weights $\lambda_{k,i}$ regulate the severity of violations during the genetic algorithm search. This formulation guides the optimization toward physically feasible HFT designs without excluding near-feasible solutions in early generations.

Table 4. Penalty weights (applied to all three objectives)

Constraint	Normalization $\hat{g}_i$	Weight $\lambda_{k,i}$
(C1) $\eta \geq 0.99$	$(0.99 - \eta)/0.99$	10^3
(C2) $\Delta T \leq T_{max}$	$(\Delta T - T_{max})/T_{max}$	10^3
(C3) $\lvert L_{\text{Total}} - L_{\text{DAB}} \rvert \leq 0.1 L_{\text{DAB}}$	$\big(\lvert L_{\text{Total}} - L_{\text{DAB}} \rvert / (0.1 L_{\text{DAB}}) - 1\big)$	10^3
(C4) $A_{wt} \leq 0.6 A_w$	$(A_{wt}/(0.6A_w) - 1)$	10^3
(C5)$r_o \leq \delta$ with $r_o \equiv \max\{r_{op}, r_{os}\}$	$(r_o/\delta - 1)$	10^2

6. RESULT AND DISCUSSION

The following section presents the simulation setup and numerical results obtained from the proposed GA–based optimization of the HFT. The results highlight how the proposed GA framework optimizes the transformer's efficiency, loss distribution, and design compactness while satisfying the constraints listed in Table 5. The winding window factor also plays a crucial role, as adequate space ensures better thermal dissipation, reduces copper losses, and supports higher efficiency without exceeding the permissible fill limit. The optimization outcomes demonstrate balanced trade-offs among size, efficiency, and loss components, showing the capability of the GA to converge toward physically realizable designs. The analyzed parameters further confirm that the proposed approach achieves high performance with stable convergence across multiple constraint conditions. All parameters were implemented in MATLAB to evaluate loss distribution, leakage inductance, and efficiency trade-offs.

A multi-objective GA is used for optimization due to its ability to handle non-linear and constrained problems. The GA is implemented in MATLAB with the following settings: population size = 50, mutation rate = 0.03, crossover rate = 0.8, and maximum generations = 150. The algorithm minimizes three objective functions: (i) Area product, (ii) copper losses, and (iii) core losses. Constraints are enforced using penalty functions, including limits on efficiency ($\geq 99\%$), temperature rise, leakage inductance, and winding area fill. The GA selects, mutates, and recombines solution candidates using fitness scores based on these combined objectives and penalties.

Table 5. Simulation parameters and results

Parameter	Value
Input DC voltage (V_1)	120 V
Output DC voltage (V_2)	12 V
Power rating (P_{out})	150 W
Leakage inductance (L_{DAB})	1.09×10^{-4} H
Total inductance (secondary referred, L_{Total})	6.27×10^{-4} H
Switching frequency (f)	11 kHz
Secondary leakage inductance (L_{ks})	2.79×10^{-4} H
Primary leakage inductance (L_{kp})	3.48×10^{-6} H
Primary AC resistance (R_{pac})	$1.23 \times 10^{-4}\,\Omega$
Secondary AC resistance (R_{sac})	$1.68 \times 10^{-6}\,\Omega$
Efficiency of HFT (η)	99.87%

In order to improve the HFT's design parameters while taking efficiency, temperature, and leakage inductance limitations into account, the GA is utilized. Outcomes of the simulation are displayed in Table 5:

– When it comes to the area product, the Pareto optimal front would display trade-offs between it and other goals. Reducing the area product may result in more losses or lower efficiency, and vice versa, as a Pareto front could illustrate.

– Losses, particularly those involving copper and iron, are the subject of the second objective function. For this goal, the Pareto front would show the trade-offs between reducing iron losses and copper losses. It could indicate that lowering one kind of loss could lead to a rise in the other, or vice versa.

Table 6 presents selected values of objective functions and design variables obtained through the process of optimization using the GA in MATLAB. The table depicts trade-offs among three principal objectives: minimization of area product f_1, minimization of total losses f_2 and f_3—of copper and core—and optimal utilization of winding area. The corresponding efficiencies η always possess high values throughout the solutions, above 99.87%. In particular, copper and iron losses oscillations demonstrate the intrinsic trade-off: attempts to mitigate one type of loss will increase the other.

Table 6. Values of objective functions, variables, and efficiency from GA optimization

x_1 (T)	x_2 (Hz)	x_3 (A/m^2)	$A_p = f_1$ (m^4)	$P_{cu} = f_2$ (W)	$P_{fe} = f_3$ (W)	η_{tr} (%)
2.96×10^{-1}	1.18×10^{4}	2.63×10^{6}	1.09×10^{-7}	1.71×10^{-3}	2.18×10^{-1}	99.85
2.92×10^{-1}	1.19×10^{4}	4.61×10^{6}	1.10×10^{-7}	1.60×10^{-3}	2.15×10^{-1}	99.86
3.15×10^{-1}	1.08×10^{4}	3.89×10^{6}	1.12×10^{-7}	1.63×10^{-3}	2.30×10^{-1}	99.85
2.70×10^{-1}	1.25×10^{4}	5.20×10^{6}	1.13×10^{-7}	1.61×10^{-3}	1.98×10^{-1}	99.87
3.02×10^{-1}	1.11×10^{4}	4.92×10^{6}	1.14×10^{-7}	1.62×10^{-3}	2.20×10^{-1}	99.85
2.80×10^{-1}	1.18×10^{4}	4.12×10^{6}	1.16×10^{-7}	1.67×10^{-3}	2.04×10^{-1}	99.86
3.05×10^{-1}	1.07×10^{4}	4.98×10^{6}	1.18×10^{-7}	1.65×10^{-3}	2.20×10^{-1}	99.85

In this study, the PSO algorithm is executed in MATLAB under the same design constraints and objective functions as GA. The PSO settings included a swarm size of 50, an inertia weight of 0.7, cognitive and social coefficients set to 1.5, and a maximum of 150 generations. The resulting solutions, shown in Table 7, highlight PSO's capability to find efficient transformer designs; however, compared to GA, the designs tend to yield slightly higher total losses and area products.

Table 7. Values of objective functions variables from PSO optimization

x_1 (T)	x_2 (Hz)	x_3 (A/m^2)	$A_p = f_1$ (m^4)	$P_{cu} = f_2$ (W)	$P_{fe} = f_3$ (W)	η_{tr} (%)
3.01×10^{-1}	1.15×10^{4}	4.55×10^{6}	1.15×10^{-7}	1.75×10^{-3}	2.26×10^{-1}	99.85
2.98×10^{-1}	1.17×10^{4}	4.21×10^{6}	1.13×10^{-7}	1.67×10^{-3}	2.19×10^{-1}	99.85
3.07×10^{-1}	1.06×10^{4}	5.10×10^{6}	1.17×10^{-7}	1.70×10^{-3}	2.24×10^{-1}	99.85
2.85×10^{-1}	1.22×10^{4}	4.30×10^{6}	1.14×10^{-7}	1.69×10^{-3}	2.17×10^{-1}	99.86
3.00×10^{-1}	1.10×10^{4}	4.90×10^{6}	1.16×10^{-7}	1.72×10^{-3}	2.21×10^{-1}	99.85
3.04×10^{-1}	1.08×10^{4}	5.00×10^{6}	1.18×10^{-7}	1.74×10^{-3}	2.25×10^{-1}	99.85
2.95×10^{-1}	1.19×10^{4}	4.60×10^{6}	1.12×10^{-7}	1.66×10^{-3}	2.18×10^{-1}	99.85

One of the most important performance metrics for any transformer is efficiency. The efficiency Pareto front would show the trade-off between increasing efficiency and reducing losses or Area product. The Pareto optimum fronts offer important information about the trade-offs present in the HFT's design space. These fronts help in making well-informed choices according to their objectives and needs. For instance, they might select a solution for f_2 that is closer to the Pareto front if minimizing losses is of the highest priority. On the other hand, they might concentrate on solutions that are closer to the Pareto front for f_1, if shrinking the Area product is the main objective. The Pareto fronts provide flexibility in developing transformers that balance several goals by allowing the exploration of a variety of workable solutions.

The Pareto optimum fronts for f_1, f_2, and f_3 offer a thorough comprehension of the trade-offs associated with HFT design optimization. Figures 5(a) and 5(b) show the 3D Pareto optimal front illustrating trade-offs between Area product, losses, and efficiency in GA and PSO-based HFT Optimization. They are an effective tool for navigating the intricate design space and making defensible choices that satisfy limitations and achieve desired goals.

Table 8 presents a direct comparison of the best results from GA and PSO optimization techniques. While both methods achieve near-identical efficiencies (99.87% for GA vs. 99.85% for PSO), GA outperforms PSO in terms of minimizing core and copper losses and convergence reliability.GA shows slightly lower total loss and faster convergence with better Pareto diversity than PSO under identical constraint conditions.

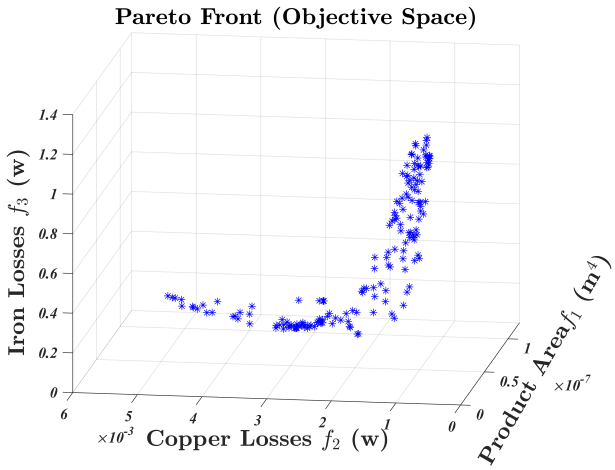

(a)

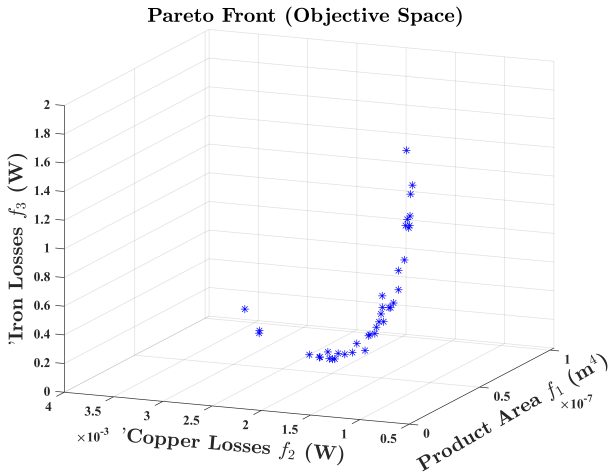

(b)

Figure 5. Three-dimensional Pareto front showing trade-offs between: f_1 – area product A_p (m^4), f_2 – Copper loss P_{cu} (W), f_3 -Iron loss P_{fe} (W) for (a) GA-based and (b) PSO based HFT optimization

Table 8. Comparison between GA and PSO optimization results

Parameter	GA	PSO
Efficiency η_{tr} (%)	99.87	99.85
Area product A_p (m^4)	1.09×10^{-7}	1.14×10^{-7}
Core loss P_{fe} (W)	0.198	0.217
Copper loss P_{cu} (W)	0.00161	0.00169
Total loss $P_T = P_{cu} + P_{fe}$ (W)	0.19961	0.21869
Convergence reliability	High	Moderate
Solution diversity	High	Moderate

Figure 6 illustrates the Pareto front comparison between GA and PSO in terms of total losses (core + copper) versus area product. Each point represents a feasible, optimized solution. GA shows a more favorable Pareto front, achieving lower total losses at smaller area products. This suggests better trade-off handling and constraint satisfaction in HFT design. By contrast, PSO showed faster initial convergence but often settled at suboptimal solutions, particularly when multiple constraints are applied. The graph demonstrates GA's superiority in exploring the design space more effectively for multi-objective optimization.

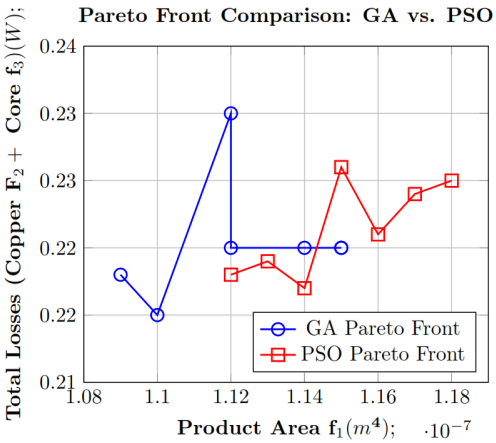

Figure 6. Pareto front comparison between GA and PSO

Core selection directly affects both the performance and efficiency of the high-frequency transformer. This choice is guided by the outcomes of the genetic algorithm optimization, with particular emphasis on the winding window area A_w. From the optimized designs, a solution with $A_w = 4.30 \times 10^{-4}\,\mathrm{m}^2$ is identified and taken as a reference for core selection. Commercially available cores are then evaluated against this requirement, and a core with a closely matching window area is selected, as shown in Table 9.

Table 9. Comparison of GA-derived and selected core parameters

Parameter	GA-derived value (m)	Selected core value (m)
Winding window area (A_w)	4.30×10^{-4}	4.37×10^{-4}
Core area (A_c)	2.69×10^{-4}	2.68×10^{-4}
Core width (C_w)	1.39×10^{-2}	2.91×10^{-2}
Core depth (C_d)	1.94×10^{-2}	1.48×10^{-2}
Core height (C_h)	8.36×10^{-2}	7.43×10^{-2}
Core outer limb width (C_{ow})	6.93×10^{-3}	9.10×10^{-3}
Winding window width (W_w)	6.93×10^{-3}	6.98×10^{-3}
Winding window height (H_w)	6.21×10^{-2}	4.35×10^{-2}

Table 10 lists the objectives and constraints used in the genetic algorithm optimization of the HFT. Efficiency, total losses, and area product were treated as the main objectives. Leakage inductance, temperature rise, and fill factor were enforced as constraints to ensure a feasible and manufacturable design with acceptable thermal behavior. The optimized results indicate that the GA achieved high efficiency with low copper and core losses. Window utilization remained within the allowable limit while satisfying magnetic and thermal margins. The secondary-referred leakage inductance of $6.27 \times 10^{-4}\,\mathrm{H}$ matches the energy transfer requirement of the DAB converter, indicating appropriate magnetic coupling. Low winding resistance and high overall efficiency further support the suitability of the GA-optimized transformer design.

Table 10. Summary of optimized objectives and constraints

Parameter	Constraint/range	Objective relation	Optimized value (GA)
Efficiency η_{tr}	$\geq 99\%$	Maximize	99.87%
Area product A_p	Minimize	Compactness	$2.96 \times 10^{-1}\,\mathrm{m}^4$
Core loss P_c	$\leq 0.002\,\mathrm{W}$	Minimize	0.198 W
Copper loss P_{cu}	$\leq 0.25\,\mathrm{W}$	Minimize	0.218 W
Leakage L_k	$1.09 \times 10^{-4}\,\mathrm{H} \pm 10\%$	Maintain ZVS	$6.21 \times 10^{-4}\,\mathrm{H}$
Temperature rise ΔT	$\leq 45\,^{\circ}\mathrm{C}$	Thermal limit	$41.2\,^{\circ}\mathrm{C}$
Fill factor k_u	≤ 0.6	Cooling margin	0.56

For copper at $f = 11$ kHz ($\rho = 1.72 \times 10^{-8}$ Ωm, $\mu_r = 1$), the skin depth in copper is ≈ 0.63 mm. Based on the skin-depth constraint, the strand diameter is selected in the range $d_{\text{strand}} = 0.3$–0.6 mm. This choice satisfies $d_{\text{strand}} \leq \delta$ and limits both skin and proximity losses. A frequency variation of $\pm 20\%$ alters δ by only $\mp 9\%$, indicating that the selected strand size remains valid over the operating range. For the secondary winding implemented using foil conductors, the thickness of each layer is restricted to $t_{\text{foil}} \leq 0.5\delta$. This constraint reduces proximity effects and keeps the AC resistance within acceptable limits. Overall, the Dowell-based loss model, combined with fill-factor constraints, provides a realistic estimate of frequency-dependent winding losses. These constraints also ensure that the winding design remains manufacturable under practical fabrication limits.

7. SIMULATION OF DAB CONVERTER WITH HFT

A detailed simulation study is carried out for a dual active bridge (DAB) converter integrated with an optimized high-frequency transformer. The simulation evaluates GA-based HFT performance by examining voltage and current waveforms, power transfer efficiency, and soft-switching behavior, using MATLAB-based results obtained from the GA-optimized HFT.

Figure 7(a) presents the main electrical waveforms obtained from the simulation, illustrating the operating behavior of the transformer and its associated components. The primary voltage V_p shows a symmetric square waveform with high peak levels, which is characteristic of full-bridge inverter operation on the high-voltage side. The corresponding secondary voltage V_s appears as a square waveform of reduced magnitude due to the transformer turns ratio, confirming effective energy transfer to the low-voltage side. The inductor current I_L, associated with the secondary leakage inductance, follows a triangular waveform characteristic of continuous conduction mode, which supports zero-voltage switching and limits switching losses. These observations confirm that the designed HFT enables efficient bidirectional power transfer and soft-switching operation within the DAB converter under realistic switching and loading conditions.

Figure 7(b) shows the output voltage V_2 response for a 1 Ω load under closed-loop operation of the DAB converter. In the simulation, V_2 is governed by the combined effects of the load resistance R_L, the effective leakage inductance L_{DAB}, and the duty ratio. The total leakage inductance L_{Total} used in the model is obtained from the GA-based optimization performed in MATLAB and is retained to enable full power transfer. Over a wide load range of 0.9–106 Ω, the closed-loop response maintains V_2 close to 12 V, indicating stable load regulation. As R_L decreases below 1 Ω, the rising load current limits the control margin and voltage regulation begins to deteriorate. Under these conditions, the duty cycle d approaches its upper limit of 0.5, indicating the practical operating boundary of the converter.

The PI controller adjusts the control action to compensate for load variations and maintain output voltage stability. Output regulation is primarily determined by the phase-shift ratio d and the input voltage V_1, both adjusted through the PI control loop. Boundary analysis identifies a minimum allowable load resistance of approximately 0.9 Ω and a duty-cycle limit of 0.5, which together define the operational constraints of the DAB converter.

The DAB stage is operated under single phase-shift (SPS) control. The primary and secondary full bridges synthesize square voltages of amplitudes V_1 and V_2, with a relative phase shift $\phi = \pi d$, $d \in [0, 0.5]$. The series inductance participating in energy transfer is L_{DAB} (all inductances referred to the *secondary* side in this study), and the transformer turns ratio is $n = N_s/N_p$.

A discrete PI controller regulates the measured V_2 to $V_2^\star = 12$ V by commanding $d \in [0, 0.5]$ as (51).

$$d[k] = \text{sat}_{[0,\,0.5]} \left\{ d[k-1] + K_p\big(V_2^\star - V_2[k]\big) + K_i T_s \sum_{j=0}^{k} \big(V_2^\star - V_2[j]\big) \right\} \tag{51}$$

With sampling at the switching period $T_s = 1/f_s$. A conservative bandwidth of ≈ 300 Hz is used; in our model $K_p = 0.06$, $K_i = 180\,\text{s}^{-1}$. The feasible region is ultimately set by (51) and by ZVS constraints via i_L sign; when d hits 0.5 the loop saturates, defining the low-R_L boundary.

For SPS control, the DAB steady-state power follows the standard relation given in (36). Using this expression, the required phase-shift $\phi = \pi d$ is obtained by equating the transferred power P to the load demand $P_{\text{req}} = (V_2^\star)^2/R_L$. This yields a quadratic form in ϕ, whose feasible solution $d = \phi/\pi$ determines the operating point. With $V_1 = 120$ V, $V_2^\star = 12$ V, $n = 0.1$, $f_s = 11$ kHz, and $L_{\text{DAB}} = 1.09$ mH, the converter achieves $P_{\max} \approx 150$ W and maintains voltage regulation for $R_L \geq 0.96$ Ω.

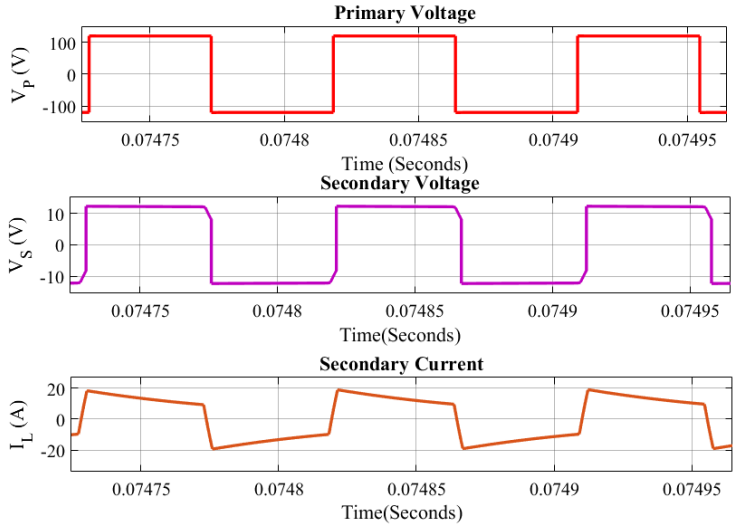

(a)

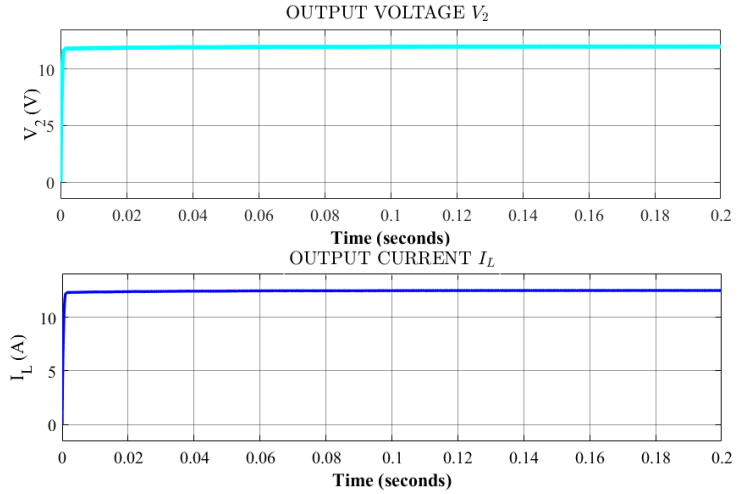

(b)

Figure 7. Simulation results of the GA-optimized HFT in closed-loop DAB operation: (a) HFT waveforms v_p, v_s, i_L and (b) regulated V_2 and I_L for $R_L = 1\ \Omega$

8. CONCLUSION

This research paper describes a novel approach for constructing HFTs for DAB converters within SSTs utilizing GAs. The proposed GA approach differs from previous thermal–electromagnetic optimization approaches by jointly constraining efficiency, leakage inductance, temperature rise, and window utilization, thereby producing compact, manufacturable transformer geometries validated through MATLAB-based DAB simulation. The inclusion of all the above constraints which is rarely integrated in previous works and it makes this approach novel and better suited for high-performance SST designs. The simulation results, which include the production of Pareto optimal fronts, indicate the feasibility and usefulness of the suggested methodology for navigating the complicated design space and determining ideal HFT configurations. A comparison with PSO further confirmed that the GA yields more balanced and efficient HFT designs under multiple constraints. Finally, this study provides a useful tool for designing high-performance, small, and dependable HFTs, which are critical for the growth of SST technology in modern power systems.Future work will extend the proposed optimization to include hybrid GA–AI approaches for faster convergence and real-time adaptation. Cost-oriented objectives and three-phase SST applications will also be explored to further enhance the practicality and scalability of the design approach.

ACKNOWLEDGMENTS

The authors gratefully acknowledge the financial support from the Student Startup and Innovation Policy (SSIP) at A.D. Patel Institute of Technology, New Vallabh Vidyanagar, India.

FUNDING INFORMATION

This research received no specific grant from any funding agency in the public, commercial, or not-for-profit sectors.

AUTHOR CONTRIBUTIONS STATEMENT

This journal uses the Contributor Roles Taxonomy (CRediT) to recognize individual author contributions, reduce authorship disputes, and facilitate collaboration.

Name of Author	C	M	So	Va	Fo	I	R	D	O	E	Vi	Su	P	Fu
Jayrajsinh B. Solanki	✓	✓	✓	✓	✓	✓		✓	✓	✓	✓			
Kalpesh J. Chudasama		✓		✓	✓		✓			✓	✓	✓	✓	

C	: **C**onceptualization	I	: **I**nvestigation	Vi	: **Vi**sualization
M	: **M**ethodology	R	: **R**esources	Su	: **Su**pervision
So	: **So**ftware	D	: **D**ata Curation	P	: **P**roject Administration
Va	: **Va**lidation	O	: Writing - **O**riginal Draft	Fu	: **Fu**nding Acquisition
Fo	: **Fo**rmal Analysis	E	: Writing - Review & **E**diting		

CONFLICT OF INTEREST STATEMENT

The authors declare that there is no conflict of interest regarding the publication of this paper.

DATA AVAILABILITY

The data that support the findings of this study are available from the corresponding author upon reasonable request.

REFERENCES

[1] N. Verma, N. Singh, and S. Yadav, "Solid state transformer for electrical system: challenges and solution," in *2018 2nd International Conference on Electronics, Materials Engineering & Nano-Technology (IEMENTech)*, May 2018, pp. 1–5, doi: 10.1109/IEMENTECH.2018.8465315.

[2] A. Abu-Siada, J. Budiri, and A. Abdou, "Solid state transformers topologies, controllers, and applications: state-of-the-art literature review," *Electronics*, vol. 7, no. 11, p. 298, Nov. 2018, doi: 10.3390/electronics7110298.

[3] J. E. Huber and J. W. Kolar, "Solid-state transformers: on the origins and evolution of key concepts," *IEEE Industrial Electronics Magazine*, vol. 10, no. 3, pp. 19–28, Sep. 2016, doi: 10.1109/MIE.2016.2588878.

[4] M. A. Shamshuddin, F. Rojas, R. Cardenas, J. Pereda, M. Diaz, and R. Kennel, "Solid state transformers: concepts, classification, and control," *Energies*, vol. 13, no. 9, p. 2319, May 2020, doi: 10.3390/en13092319.

[5] M. M. Rana *et al.*, "Comprehensive review on the charging technologies of electric vehicles (EV) and their impact on power grid," *IEEE Access*, vol. 13, pp. 35124–35156, 2025, doi: 10.1109/ACCESS.2025.3538663.

[6] H. Bai and C. Mi, "Eliminate reactive power and increase system efficiency of isolated bidirectional dual-active-bridge DC-DC converters using novel dual-phase-shift control," *IEEE Transactions on Power Electronics*, vol. 23, no. 6, pp. 2905–2914, 2008, doi: 10.1109/TPEL.2008.2005103.

[7] H. Rahbarimagham and G. B. Gharehpetian, "The effect of smart transformers on the optimal management of a microgrid," *Electric Power Systems Research*, vol. 238, p. 111044, Jan. 2025, doi: 10.1016/j.epsr.2024.111044.

[8] A. Zahernia and H. Rahbarimagham, "Application of smart transformers in power systems including PV and storage systems under unbalanced and nonlinear load and fault condition," *Electric Power Systems Research*, vol. 201, p. 107535, Dec. 2021, doi: 10.1016/j.epsr.2021.107535.

[9] C. Leung, S. Dutta, S. Baek, and S. Bhattacharya, "Design considerations of high voltage and high frequency three phase transformer for solid state transformer application," in *2010 IEEE Energy Conversion Congress and Exposition*, Sep. 2010, pp. 1551–1558, doi: 10.1109/ECCE.2010.5618234.

[10] M. A. Hannan *et al.*, "State of the art of solid-state transformers: advanced topologies, implementation issues, recent progress and improvements," *IEEE Access*, vol. 8, pp. 19113–19132, 2020, doi: 10.1109/ACCESS.2020.2967345.

[11] J. B. Solanki and K. J. Chudasama, "Concepts, configurations, and challenges of solid-state transformer: a review," *Recent Advances in Electrical & Electronic Engineering (Formerly Recent Patents on Electrical & Electronic Engineering)*, vol. 15, no. 5, pp. 348–368, Aug. 2022, doi: 10.2174/2352096515666220707120302.

[12] U. Tahir *et al.*, "Design of three phase solid state transformer deployed within multi-stage power switching converters," *Applied Sciences*, vol. 9, no. 17, p. 3545, Aug. 2019, doi: 10.3390/app9173545.

[13] P. Garcia, S. Saeed, A. Navarro-Rodriguez, J. Garcia, and H. Schneider, "Switching frequency optimization for a solid state transformer with energy storage capabilities," *IEEE Transactions on Industry Applications*, vol. 54, no. 6, pp. 6223–6233, Nov. 2018, doi: 10.1109/TIA.2018.2860561.

[14] C. W. T. McLyman, *Transformer and inductor design handbook*. CRC Press, 2017, doi: 10.1201/b10865.

[15] T. Hagawane, M. R. Sindhu, and R. Patankar, "Model predictive control of dual active bridge DC-DC converter based on PWM plus TPS modulation for automotive applications," *2022 International Virtual Conference on Power Engineering Computing and Control: Developments in Electric Vehicles and Energy Sector for Sustainable Future (PECCON)*, 2022, pp. 1–6, doi: 10.1109/PECCON55017.2022.9851171.

[16] O. Ibrahim *et al.*, "Parametric modelling of phase-shifted full-bridge zero voltage switching DC-DC converter," *Jordan Journal of Electrical Engineering*, vol. 7, no. 1, p. 71, 2021, doi: 10.5455/jjee.204-1601668266.

[17] M. Mogorovic and D. Dujic, "Medium frequency transformer leakage inductance modeling and experimental verification," in *2017 IEEE Energy Conversion Congress and Exposition (ECCE)*, Oct. 2017, pp. 419–424, doi: 10.1109/ECCE.2017.8095813.

[18] P. Inampudi, P. Chandrasekar, and T. V. Muni, "Evaluating a novel bidirectional soft-switching DC-DC converter for electric vehicles," *International Journal of Applied Power Engineering (IJAPE)*, vol. 13, no. 4, pp. 825–834, Dec. 2024, doi: 10.11591/ijape.v13.i4.pp825-834.

[19] B. Zhao, Q. Yu, and W. Sun, "Extended-phase-shift control of isolated bidirectional DC-DC converter for power distribution in microgrid," *IEEE Transactions on Power Electronics*, vol. 27, no. 11, pp. 4667–4680, 2012, doi: 10.1109/TPEL.2011.2180928.

[20] O. Aldosari, L. A. G. Rodriguez, J. C. Balda, and S. K. Mazumder, "Design trade-offs for medium- and high-frequency transformers for isolated power converters in distribution system applications," in *2018 9th IEEE International Symposium on Power Electronics for Distributed Generation Systems (PEDG)*, Jun. 2018, pp. 1–7, doi: 10.1109/PEDG.2018.8447788.

[21] K. D. Hoang and J. Wang, "Design optimization of high frequency transformer for dual active bridge DC-DC converter," in *2012 XXth International Conference on Electrical Machines*, Sep. 2012, pp. 2311–2317, doi: 10.1109/ICElMach.2012.6350205.

[22] R. F. Hassan and K. R. Hameed, "Design of high frequency transformers in different shape of core using MATLAB program," *Indonesian Journal of Electrical Engineering and Computer Science*, vol. 20, no. 3, pp. 1159–1172, Dec. 2020, doi: 10.11591/ijeecs.v20.i3.pp1159-1172.

[23] T. O. Olowu, H. Jafari, M. Moghaddami, and A. I. Sarwat, "Multiphysics and multi objective design optimization of high-frequency transformers for solid-state transformer applications," *IEEE Transactions on Industry Applications*, vol. 57, no. 1, pp. 1014–1023, Jan. 2021, doi: 10.1109/TIA.2020.3035129.

[24] M. A. Bahmani, "Design and optimization of HF transformers for high power DC-DC applications," Ph.D. dissertation, Department of Energy and Environment Chalmers, University of Technology, Sweden, 2014. [Online]. Available: http://publications.lib.chalmers.se/records/fulltext/195670/195670.pdf.

[25] M. A. Bahmani, T. Thiringer, and M. Kharezy, "Design methodology and optimization of a medium-frequency transformer for high-power DC–DC applications," *IEEE Transactions on Industry Applications*, vol. 52, no. 5, pp. 4225–4233, Sep. 2016, doi: 10.1109/TIA.2016.2582825.

[26] S. Joseph, S. K. John, K. P. Pinkymol, J. Joseph, and K. R. M. Nair, "Multiphysics analysis of high frequency transformers used in SST with different magnetic materials," *Progress in Electromagnetics Research M*, vol. 116, pp. 129–143, 2023, doi: 10.2528/PIERM22121901.

[27] F. Lin *et al.*, "AI-based design with data trimming for hybrid phase shift modulation for minimum-current-stress dual active bridge converter," *IEEE Journal of Emerging and Selected Topics in Power Electronics*, vol. 12, no. 2, pp. 2268–2280, Apr. 2024, doi: 10.1109/JESTPE.2022.3232534.

[28] R. De Seram, K. T. Lulbadda, T. Sidhu, and S. S. Williamson, "An in-depth comparative analysis and efficiency evaluation of dual- and quad-active bridge for solid state transformer applications," in *2024 IEEE Transportation Electrification Conference and Expo (ITEC)*, Jun. 2024, pp. 1–6, doi: 10.1109/ITEC60657.2024.10598840.

[29] C. Wang, W. Han, P. Chen, J. Song, and S. Yuan, "Multiobjective optimization design of high frequency transformer based on NSGA-II algorithm," in *2022 IEEE International Conference on Mechatronics and Automation (ICMA)*, Aug. 2022, pp. 664–669, doi: 10.1109/ICMA54519.2022.9856127.

[30] C. Hernandez, J. Lara, M. A. Arjona, and E. Melgoza-Vazquez, "Multi-objective electromagnetic design optimization of a power transformer using 3D finite element analysis, response surface methodology, and the third generation non-sorting genetic algorithm," *Energies*, vol. 16, no. 5, p. 2248, Feb. 2023, doi: 10.3390/en16052248.

[31] B. Shi *et al.*, "Multi-objective optimization method for power transformer design based on surrogate modeling and hybrid heuristic algorithm," *Electronics*, vol. 14, no. 6, p. 1198, Mar. 2025, doi: 10.3390/electronics14061198.

[32] P. Su, J. Wu, Y. Li, Z. Zhao, L. Xie, and J. Liu, "Robust optimization design of high-frequency transformer considering the effects of core cutting," *Journal of Magnetics*, vol. 30, no. 3, pp. 295–306, Sep. 2025, doi: 10.4283/JMAG.2025.30.3.295.

[33] S. M. Hashemzadeh *et al.*, "A high voltage gain solid-state transformer for integration of renewable energy and AC sources," *Scientific Reports*, vol. 14, no. 1, p. 25471, Oct. 2024, doi: 10.1038/s41598-024-77326-5.

[34] W. G. Hurley and W. H. Wölfle, *Transformers and inductors for power electronics*. John Wiley & Sons, 2013, doi: 10.1002/9781118544648.

[35] G. Ortiz, J. Biela, and J. W. Kolar, "Optimized design of medium frequency transformers with high isolation requirements," in *IECON 2010 - 36th Annual Conference on IEEE Industrial Electronics Society*, Nov. 2010, pp. 631–638, doi: 10.1109/IECON.2010.5675240.

[36] R. G. Montoya, "High-frequency transformer design for solid-state transformers in electric power distribution systems," M.S. thesis, University of Arkansas, Fayetteville, USA, 2015. [Online]. Available: https://scholarworks.uark.edu/etd/1382.

[37] P. L. Dowell, "Effects of eddy currents in transformer windings," *Proceedings of the Institution of Electrical Engineers*, vol. 113, no. 8, pp. 1387–1394, 1966, doi: 10.1049/piee.1966.0236.
[38] S. Balci, I. Sefa, and N. Altin, "Design and analysis of a 35 kVA medium frequency power transformer with the nanocrystalline core material," *International Journal of Hydrogen Energy*, vol. 42, no. 28, pp. 17895–17909, Jul. 2017, doi: 10.1016/j.ijhydene.2017.03.158.
[39] G. G. Orenchak, "Estimating temperature rise of transformers," *Power Electronics Technology*, 2004. https://www.electronicdesign.com/content/article/21187276/estimating-temperature-rise-of-transformers.
[40] J. B. Solanki and K. J. Chudasama, "Design and simulation of dual active bridge converters to enhance performance of solid state transformers," in *2024 Parul International Conference on Engineering and Technology (PICET)*, May 2024, pp. 1–6, doi: 10.1109/PICET60765.2024.10716191.
[41] A. Shri, "A solid-state transformer for interconnection between the medium-and the low-voltage grid design, control and behavior analysis challenge the future," Ph.D. dissertation, Delft University of Technology, 2013. [Online]. Available: https://repository.tudelft.nl/islandora/object/uuid:3bb366d5-6f87-4636-a4a3-0245269125f5/datastream/OBJ.
[42] Y. Zhang, H. Liu, and X.Wang, "Comprehensive analysis of zvs operation range and deadband conditions in bidirectional dc–dc converters," *International Journal of Power Electronics*, vol. 15, no. 2, pp. 215–229, 2023, doi: 10.1155/2023/8882417.
[43] C. Mi, H. Bai, C. Wang, and S. Gargies, "Operation, design and control of dual H-bridge-based isolated bidirectional DC–DC converter," *IET Power Electronics*, vol. 1, no. 4, pp. 507–517, Dec. 2008, doi: 10.1049/iet-pel:20080004.
[44] V. Esteve, J. L. Bellido, J. Jordán, and E. J. Dede, "Improving the efficiency of an isolated bidirectional dual active bridge DC–DC converter using variable frequency," *Electronics (Switzerland)*, vol. 13, no. 2, 2024, doi: 10.3390/electronics13020294.
[45] R. W. A. A. De Doncker, D. M. Divan, and M. H. Kheraluwala, "A three-phase soft-switched high-power-density DC/DC converter for high-power applications," *IEEE Transactions on Industry Applications*, vol. 27, no. 1, pp. 63–73, 1991, doi: 10.1109/28.67533.
[46] M. N. Kheraluwala, R. W. Gascoigne, D. M. Divan, and E. D. Baumann, "Performance characterization of a high-power dual active bridge DC-to-DC converter," *IEEE Transactions on Industry Applications*, vol. 28, no. 6, pp. 1294–1301, 1992, doi: 10.1109/28.175280.

BIOGRAPHIES OF AUTHORS

Jayrajsinh B. Solanki is currently working as a lecturer in the Electrical Engineering Department at B. & B. Institute of Technology, Vallabh Vidyanagar, Gujarat, India. He received his B.E. degree in electrical engineering from Hemchandracharya North Gujarat University, Patan, in 2009, and his M.Tech. in electrical engineering from Nirma University, Ahmedabad, in the same year. He is presently pursuing a Ph.D. in electrical engineering from Gujarat Technological University. His research interests include SSTs, high-frequency transformer (HFT) design, power electronics, electromagnetic simulation, and optimization algorithms. He has contributed to multiple funded student innovation projects and actively mentors research work in power electronics. He also serves as a reviewer for international Scopus-indexed journals, reflecting his engagement with the global research community. His academic profile demonstrates a strong commitment to high-frequency magnetics and smart grid integration. He can be contacted at email: jayraj_ee@yahoo.co.in.

Dr. Kalpesh J. Chudasama is currently working as an associate professor in the Electrical Engineering Department at A. D. Patel Institute of Technology (ADIT), New Vallabh Vidyanagar, Gujarat, India. He earned his B.E. degree in electrical engineering from B.V.M. Engineering College under Sardar Patel University in 1997, his M.E. in electrical power systems in 2003, and his Ph.D. in electrical engineering from Gujarat Technological University in 2016. He has a total of 26 years of professional experience, including 4 years in industry and over two decades in academia. His areas of interest include solid-state power transformers, smart distribution systems, DC microgrids, fault diagnosis, and machine learning applications in power systems. Dr. Chudasama has published more than 33 research papers in reputed national/international journals and conferences. He is also an editorial board member and reviewer for several reputed journals. He can be contacted at email: ee.kalpesh.chudasama@adit.ac.in.